

Accuracy of DFT computed oxygen-vacancy formation energies and high-throughput search of solar thermochemical water-splitting compounds

Bianca Baldassarri ¹, Jiangang He ^{2,*}, Xin Qian ^{2,†}, Emanuela Mastronardo ^{2,‡}, Sean Griesemer ²,
Sossina M. Haile ^{1,2} and Christopher Wolverton ^{1,2,§}

¹Graduate Program in Applied Physics, Northwestern University, Evanston, Illinois, USA

²Department of Materials Science and Engineering, Northwestern University, Evanston, Illinois, USA



(Received 11 March 2023; accepted 27 April 2023; published 7 June 2023)

The enthalpy change involved in metal oxide reduction is a key quantity in various processes related to energy conversion and storage and is of particular interest for computational prediction. Often this prediction involves the simulation of a high-temperature reduction process with a 0-K methodology like density functional theory (DFT), and it is not infrequent for the high temperature and 0-K stable crystal structures to differ. This introduces a conundrum with regard to the choice of crystal structure to utilize in the computation, with approaches in the literature varying and experimental validation remaining scarce. In this work, we address both the crystal structure conundrum and the experimental validation, and then apply the insights we gain to guide a high-throughput search for new materials for solar thermochemical water-splitting applications. By computing the DFT+ U oxygen-vacancy formation energy (ΔE_{vf}) of a selection of ABO_3 compounds and comparing different crystal structures for each composition, we highlight the issues that arise when the structure utilized in the computation is dynamically unstable at 0 K, namely the presence of an artificial lowering of ΔE_{vf} , and the lack of convergence of ΔE_{vf} with cell size. We solve these limitations by identifying and employing a suitable surrogate dynamically stable structure. We then validate the predictive power of our calculations against apositely generated experimental measurements of reduction enthalpy for a series of Hubbard U values, finding an accuracy ranging between 0.2–0.6 eV/O. In light of such conclusions, we revise and expand a previous a high-throughput DFT study on ABO_3 perovskite oxides. We provide a list of candidate STCH materials, highlight trends with redox-active cation and structural distortion, and identify Mn^{4+} , Mn^{3+} , and Co^{3+} as the most promising redox-active cations.

DOI: [10.1103/PhysRevMaterials.7.065403](https://doi.org/10.1103/PhysRevMaterials.7.065403)

I. INTRODUCTION

The thermodynamics of oxygen release from metal oxide materials are fundamental to a number of energetic processes and therefore drive materials selection for applications such as solid oxide fuel cells (SOFCs) [1,2] and solar thermochemical splitting of water and carbon dioxide [3–6]. In this context, *ab initio* methods and materials databases represent powerful tools to guide materials exploration on much larger scales than would be experimentally feasible by allowing for the screening of compounds based on specific properties of interest. However, even within large scale high-throughput density functional theory (HT-DFT) studies, complexities such as considering all relevant competing structures at each composition make a large survey challenging within a reasonable computational cost. Furthermore, simulating finite temperature phenomena, like oxygen release in solar-thermochemical

water splitting, with a 0-K methodology like DFT raises the possibility that the finite temperature structure differs from the stable one at 0 K, introducing additional complexities. As such, examining the influence of crystal structure on the properties computed in an HT-DFT screening represents a fundamental part of evaluating its predictive power.

The property at the center of the present work is the oxygen-vacancy formation energy (ΔE_{vf}), which can be utilized as a screening criterion to identify new candidate materials for a number of applications, this work in particular focusing on solar thermochemical hydrogen production (STCH). Typical STCH cycles consist of a reduction step, in which a metal oxide compound loses oxygen upon heating, and a water-splitting step, where steam is supplied to the reduced material, which reoxidizes producing hydrogen. Meredig and Wolverton have analyzed the thermodynamics of the two-step redox reaction and determined a window of values of the enthalpy change associated with the reduction reaction (ΔH_{red}) allowing for both reactions steps to be thermodynamically favourable [7]. Materials can thereby be screened for STCH applications by evaluating their thermodynamic stability and computing ΔE_{vf} to quantify ΔH_{red} [8,9].

A class of materials that has attracted significant attention for use in STCH is that of perovskites oxides. The interest in such compounds, initially sparked from promising studies on strontium-doped lanthanum manganese perovskites [10–13],

*Present: School of Mathematics and Physics, University of Science and Technology Beijing, Beijing, China.

†Present: Saint-Gobain Research North America, Massachusetts, USA.

‡Present: Engineering Department, University of Messina, Messina, Italy.

§Corresponding author: c-wolverton@northwestern.edu

is supported by a variety of attractive properties: structural stability up to high temperature, ability to withstand a large amount of oxygen loss, ease of oxygen diffusion, and a possibility for reduction at lower temperatures than Ceria, the benchmark material in the field [10,11,14,15]. Although the term “perovskite” is at times utilized somewhat broadly, the work by Breternitz and Schorr [16] provides a clear definition consisting of three specific characteristics: a ratio of 1:1:3 between the two cations and the anion (O in this case), an octahedral coordination of the B site cation, and a corner sharing octahedral network. This definition, which will be used throughout this work, encompasses a number of different distortions of the ideal cubic perovskite structure. The lower symmetry distorted phases are commonly more energetically favourable at lower temperatures, with phase transitions to the higher symmetry phases, and ultimately the cubic phase, being observed in several materials when temperature is increased [17–21].

The phase change behavior of perovskites is an example of the conundrum arising when the high temperature and the 0-K stable structure differ, and can significantly impact the computation of ΔE_{vf} . In the literature, studies computing the enthalpy change involved in oxygen release from perovskite structures differ in their approaches with regards to the choice of structures employed in the simulation. Ezbiri *et al.* [22] and Vieten *et al.* [23], for example, employed structures derived from the cubic perovskite phase and examined their reduction to the corresponding brownmillerite phases. Gautam *et al.* [24] and Wexler *et al.* [9] examined several distorted perovskite prototype structures, and introduced a vacancy in a supercell of the lowest DFT energy one. Deml *et al.* [25] and Emery *et al.* [8] created vacancy-containing supercells of, respectively, structures reported in the inorganic crystal structure database (ICSD) [26,27] and perfect cubic perovskite structures. Indeed, a number of arguments in favor of the employment of a cubic cell, particularly within high-throughput studies, can be put forth (i) its high degree of symmetry (and thus computational efficiency), (ii) some evidence supporting only a small difference in ΔE_{vf} between distortions that is comparable to experimental uncertainty [28] [8], and (iii) reports of phase transitions to cubic from more distorted phases at higher temperatures, like the ones at which STCH takes place [17–21]. As we will later detail, however, the cubic perovskite structure is often dynamically unstable at 0 K, a factor that introduces difficulties in the computation of the oxygen-vacancy formation energy.

Another factor that significantly influences the computation of ΔE_{vf} is the choice of Hubbard U parameter in DFT+ U calculations. This is especially relevant for perovskites since a large portion of stable perovskites contain $3d$ transition metal elements [8]. The overdelocalization of electrons brought about by the residual self-interaction present in exchange-correlation functionals particularly affects systems like metal oxides containing $3d$ transition metals, and the introduction of a Hubbard-like potential to the energy functional [29] is a widely used option to address this delocalization [30–34]. DFT+ U is especially useful within high-throughput applications given its ease of implementation and very limited impact on simulation times. The value of the U parameter contained in the Hubbard term is often determined empirically

and results are highly dependent not only on the element of interest, but also on its local environment, and on the quantity under consideration (e.g., lattice constant, band gap, etc.) [35]. Studies in the literature on perovskites oxides and STCH materials differ in the U values employed, often opting for a constant value across elements and oxidation states. Deml *et al.* [25], for example, applied $U = 3$ eV to all transition metals aside from $U = 5$ eV for Cu and Ag, while Ezbiri *et al.* [22] opted for the absence of a Hubbard U entirely. Gautam *et al.* [24] and Wexler *et al.*, on the other hand [9], performed SCAN+ U calculations utilizing U values based on previous results from studies on the effect of U on SCAN calculations of transition metal oxides [36,37]. Reports of significant variations in reduction energies with U [28,32] motivate us to examine the effects of U on ΔE_{vf} in more details.

In this work, we analyze both the influence of different crystal structures and that of different Hubbard U values on the oxygen-vacancy formation energy. We identify issues in the computation of ΔE_{vf} in the presence of dynamically unstable structures, and develop a strategy to address them. We then perform a detailed, quantitative comparison of our DFT+ U computational results with appositely generated experimental data of enthalpy of reduction, and find an accuracy between 0.2–0.6 eV/O. Finally, we leverage the insights gained through the above analysis to revise and expand a previous high-throughput study on perovskite oxides for STCH applications [8]. The results are presented as follows. Section III A is dedicated to the analysis of the impact of different crystal structures and Hubbard U values on DFT computed values of oxygen-vacancy formation energy and to the comparison with experimental data of reduction enthalpy, with subsections on: (i) detail on experimental data, (ii) crystal structure choice, (iii) Hubbard U choice, and (iv) comparison between simulation and experiment. Section III B is then dedicated to the high-throughput DFT study of STCH materials, with sections on (i) structures and compositions included in the study, (ii) new STCH candidates, (iii) trends with a B -site cation, and (iv) trends with structural distortion.

II. METHODOLOGY

(a) *DFT calculations.* All calculations in this work have been conducted using the Vienna *ab initio* simulation package (VASP) [38,39], with projector augmented wave (PAW) potentials [40] and the Perdew-Burke-Ernzerhof (PBE) [41] generalized gradient approximation (GGA) for the exchange-correlation functional. The DFT calculations are split into two categories: low-throughput calculations for comparison with experiment (Sec. III A), and high-throughput calculations for the search of new STCH compounds (Sec. III B). The low-throughput calculations used for experimental comparison were performed using a gamma centered k -point grid with a density of at least 8600 points per reciprocal atom, and a plane wave cutoff energy of 520 eV. Self-consistency was achieved when energies of subsequent iterations differed by less than 10^{-6} eV/cell, and, ionic relaxation was performed until forces were found to be below 0.01 eV/Å. For all ABO_3 compounds in Fig. 1, additional calculations of the vacancy formation energy were performed with a plane wave cutoff of energy 800 eV, and relaxing until forces were below

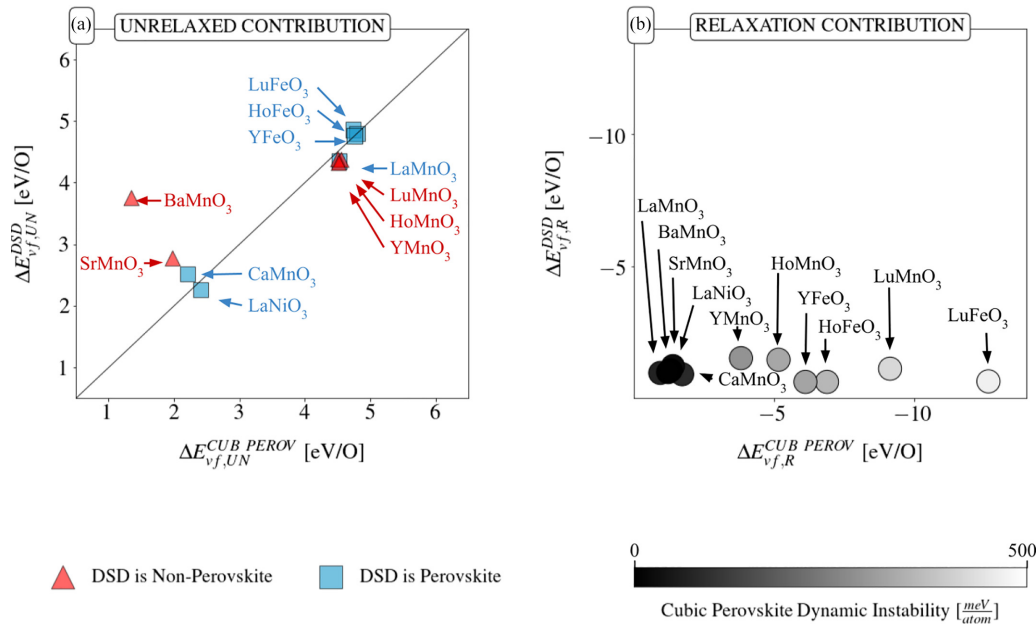


FIG. 1. Contributions to the DFT-calculated oxygen-vacancy formation energy utilizing the cubic and DSD structures: (a) energy of removing an O atom without allowing for ionic relaxation upon vacancy formation [Eq. (4)] and (b) energy difference between the relaxed and unrelaxed vacancy-containing structures [Eq. (5)]. Increasing lightness in the data points color in (b) indicates increase in the degree of dynamic instability of the cubic structure, quantified by taking the DFT energy difference between the cubic and the lowest energy perovskite distortion for each compound. In (a), different colors/shapes indicate whether the structures belong to the perovskite family. U values are those employed in the OQMD and vacancy-containing supercells are of 119 atoms for BaMnO_3 , LuMnO_3 , YMnO_3 and HoMnO_3 , and 79 atoms for all others.

0.001 eV/Å. In all cases, we observed a difference in the oxygen-vacancy formation energies of less than 0.02 eV/O compared to the 520 eV plane wave cutoff and 0.01 eV/Å force threshold (see Fig. S1 in Ref. [42]). High-throughput calculations, were performed within the OQMD framework; details on calculation settings are provided in Refs. [43,44]. While no compound selection based on charge balance was performed, the oxidation state of each cation was determined using bond valence parameters as implemented in PYMATGEN [45] and used to exclude a small number of compounds for which the oxidation state specific potential applied in the OQMD framework differed from the oxidation state of the element in the compound at hand (an occurrence relevant only for a number of rare-earth elements).

For compounds containing 3d transition metals or actinides, the overdelocalization of electrons due to the residual self interaction present in exchange-correlation functionals [30–34] was treated through the addition of a Hubbard-like potential to the energy functional [29] (DFT+U). Within the framework of the OQMD, and thus for the high-throughput calculations, the U values are fixed to the ones assigned following the work by Wang *et al.* [32]. In the low-throughput section, the influence of different U values on the vacancy formation energy of each compound was studied, and a “best-fit” U was determined for Mn^{3+} , Mn^{4+} , Fe^{3+} , Co^{3+} , and Ni^{3+} . Comparisons between DFT calculations of vacancy formation energies and experimental results of enthalpies of reduction are then provided for several sets of Hubbard U values: the “best-fit U” values, OQMD U values, and a constant value of $U = 4$ eV for all transition metal elements (see Sec. III A and Ref. [42]). Any calculation in the OQMD involving 3d

(Sc-Cu) or actinide elements applies a spin polarization with a ferromagnetic configuration, initializing magnetic moments to $5\mu_B$ (transition metals) and $7\mu_B$ (actinides). Ferromagnetic configurations were also adopted for all low-throughput calculations for the following reasons: (i) oxygen loss being measured at temperatures higher than spin ordering [46,47], (ii) evidence of the limited influence of magnetic configuration on both bulk and defect DFT energies [48], and (iii) in order to maintain consistency with high throughput. For Co-containing compounds, a low-spin configuration (where magnetic moments are initialized to $0\mu_B$ for all Co atoms aside from the two neighboring the O vacancy in the vacancy-containing cell, which are initialized to $1\mu_B$) was utilized consistently for low-throughput calculations, while a high-spin configuration (i.e. all transition metal magnetic moments initialized to $5\mu_B$) was used for high-throughput calculations due to the aforementioned settings applied in the OQMD framework.

(b) *Stability and oxygen-vacancy formation energy.* The 0-K stability (ΔE_{stab}) of each ABO_3 compound was calculated by taking the energetic difference between the OQMD convex hull energy at the composition of interest and the compound’s vacancy formation energy (ΔE_f), defined as (for an ABO_3 metal oxide):

$$\Delta E_f = E(\text{ABO}_3) - E_A - E_B - 3E_O, \quad (1)$$

where $E(\text{ABO}_3)$ indicates the DFT energy of a bulk metal oxide cell, and E_i the DFT energy of element i , and the units of ΔE_f are eV/atom. The DFT energies of elements correspond to the (per atom) energy of the DFT ground-state structure for the element under consideration, with corrections applied

to a number of elements, see Ref. [44] for details on such corrections.

The oxygen-vacancy formation energy (ΔE_{vf}) was then determined by removing an oxygen atom from a supercell of the relevant bulk structure and computed as follows:

$$\Delta E_{vf} = E(A_n B_n O_{3n-1}) + E_O - nE(ABO_3), \quad (2)$$

where $E(ABO_3)$ indicates the DFT energy of a bulk metal oxide unit cell, $E(A_n B_n O_{3n-1})$ that of a supercell n times the size of the bulk unit cell and containing one oxygen vacancy, E_O is the DFT energy of oxygen, and the units of ΔE_{vf} are eV/O. For all compounds, we calculated the oxygen-vacancy formation energy for each unique oxygen site, and report the lowest one. For compounds calculated in low-throughput and compared with experimental data, we used the experimentally synthesized structure when dynamically stable, and a dynamically stable distortion otherwise, as described in Sec. III A. For compounds in the high-throughput study, we used the ground-state structure in the OQMD, as detailed in Sec. III B. We performed convergence testing with respect to the size of the defect-containing cell for the main prototype structures involved in the high-throughput study (see Sec. III A and Fig. S6), decorated with elements belonging to several different groups. As shown in Fig. S2, the majority of compounds investigated are already converged to less than 0.1 eV/O at the smallest cell dimension considered, and, for the remaining ones, the change in oxygen-vacancy formation energy with cell size is comparable to experimental uncertainty [49–53]. Based on these observations, for all low-throughput simulation to compare with experiment we use vacancy-containing supercells with a minimum of 79 atoms to maximize accuracy, while for the high-throughput simulations, in the interest of computational efficiency, we construct supercells only when the bulk structures contain less than 15 atoms.

(c) *DFT energy of oxygen.* The lack of accuracy in the DFT energies of diatomic molecules requires the addition of an empirical correction to the DFT energy of the O_2 molecule, and hence to the reference energy (E_O) of Eqs. (1) and (2). Such correction is generally determined by fitting formation energies of oxides to experimental data [32,48,54–56], leading to a range of results depending on the data set utilized for the fit. Wang *et al.* [32], Lee *et al.* [48], and Grindy *et al.* [55] have each selected a set of binary oxides of known structure, eliminating transition metal oxides due to further complexities associated with the use of DFT+ U , and obtained similar values for E_O : -4.25 eV for Refs. [32,48] (which utilized the same set of seven binary oxides) and -4.33 eV for Ref. [55] (where the pool was expanded to 15). Figure S3 illustrates the result of the fit of 13 of the 15 oxides in Grindy’s work, performed with the same settings as the low-throughput calculations in this work, as well as with OQMD data, leading to a value of $E_O = -4.29$ eV in both cases. The value of the oxygen DFT reference energy of -4.52 eV employed in the OQMD framework was, however, determined by performing simultaneous fits of several elements (as detailed in Kirklin *et al.* [44]), with a data set comprising all OQMD entries for which experimental formation energy data was available. Arguments supporting either extreme of the range of values provided can be formulated, from the breadth of the data included in the OQMD approach, to the reliability gained

by avoiding multiple concurrent fittings when restricting to nontransition metal binary oxides only. Figure S4 displays the result of a third fit, which aims to exploit the advantages of both the aforementioned strategies by limiting the data set to a few hundred oxides not containing any of the elements that have a correction applied to their DFT elemental energy, and leads to a yet different result of -4.43 eV. In light of the above discussion, we consider the choice of oxygen DFT reference energy value to introduce an additional complexity in the comparison between computation and experiment presented in Sec. III A. For the present work, in the interest of consistency between high- and low-throughput data, we employ the OQMD value of $E_O = -4.52$ eV for all calculations, and emphasize the presence of an associated uncertainty of about 0.2 eV. We note that a change in the empirical correction factor for O_2 would result in a constant shift of all vacancy formation energies, i.e., the difference between two vacancy formation energies would be unaffected by this correction.

(d) *Dynamic stability.* In order to determine the 0-K dynamic stability of the compounds investigated in Sec. III A, the phonon dispersion was calculated by means of the finite difference method as implemented in PHONOPY [57] utilizing $2 \times 2 \times 2$ supercells ($2 \times 2 \times 1$ for cases in which the original cell contained 30 atoms). The presence of imaginary frequencies in the phonon band structure was considered as evidence of dynamic instability. The degree of instability was quantified with the energetic difference between the unstable phase and its lowest energy dynamically stable distortion on the OQMD, which we found to be positively correlated with the largest imaginary phonon frequency, as shown for a selected number of cubic perovskites in Fig. S5.

(e) *Charge localization.* The charge localized on each atom in the perfect bulk structure was determined through Bader charge analysis as implemented in PYMATGEN [45]. After the introduction of a neutral oxygen vacancy, the charge localization on each atom in the defect-containing structure was determined in the same fashion. The charge localization upon vacancy formation was then calculated by taking the difference in the charge localized on each atom in the defect-containing cell and in the perfect bulk cell. The charge localized upon vacancy formation was then summed over all atomic sites for each of the two cation species in each ABO_3 compound, thus obtaining a total Δq_A and Δq_B . The reducing (or redox-active) cation was then labeled based on the larger of the two Δq . We note that the nature of this labeling is approximate and not univocal; for example, for perovskite oxides, while the reducing cation coincides with the B site cation in the vast majority of cases, evidence of possible reduction of both A and B sites is present in a few cases.

III. RESULTS

A. Comparison of DFT calculations and experimental measurements of oxygen-vacancy formation energy

In order to assess the accuracy of DFT in guiding materials search based on reduction thermodynamics, we begin by performing a detailed quantitative comparison between DFT ΔE_{vf} and experimental measurements of oxide reduction enthalpies. As mentioned in the introduction, this comparison is

TABLE I. List of experimentally synthesized compounds on which TGA measurements were performed and the structures and energy differences of the structures of interest, from left to right: experimentally observed crystal structures (EXP) (if a phase transition was observed the high-temperature structure is also reported, and the transition is indicated with an arrow) [46,47], dynamically stable distortions (DSD), ground-state structures on the OQMD (DFT GS), energy difference between the cubic perovskite phase and the ground-state structure on the OQMD [$\Delta E(\text{CUB PEROV-DFT GS})$], and energy difference between the experimentally observed structure and the dynamically stable distortion [$\Delta E(\text{EXP-DSD})$]. Perovskite structures are indicated with “perov” and the crystal system of the distortion of interest (for example, for YFeO_3 the DFT GS structure is an orthorhombic perovskite with GdFeO_3 prototype, which is indicated as “ortho perov”), while nonperovskite structures are indicated using the name of the prototype structure on ICSD (for example, LuMnO_3 , YMnO_3 , and HoMnO_3 have, in all three cases, a DSD structure with the same hexagonal structure as prototype: “ LuMnO_3 ”). A visualization of these crystal structures is provided in Figs. S6 and S7. For all structures the space group is reported in parenthesis.

Formula	EXP structure	DFT DSD structure	DFT GS structure	ΔE	ΔE
				(CUB PEROV -DFT GS)	(EXP- DSD)
				$\frac{\text{meV}}{\text{atom}}$	$\frac{\text{meV}}{\text{atom}}$
PrCoO_3	ortho perov ($Pnma$)	ortho perov ($Pnma$)	ortho perov ($Pnma$)	94	–
SmCoO_3	ortho perov ($Pnma$)	ortho perov ($Pnma$)	ortho perov ($Pnma$)	168	–
LaCoO_3	rhom perov ($R\bar{3}c$)	rhom perov ($R\bar{3}c$)	monocl perov ($P2_1/c$)	86	–
CaMnO_3	ortho perov ($Pnma$) \rightarrow cub perov ($Pm\bar{3}m$)	ortho perov ($Pnma$)	ortho perov ($Pnma$)	101	–
SrMnO_3	“ BaMnO_3 ” ($P6_3/mmc$)	“ CsCuBr_3 ” ($C222_1$)	“ CsCuBr_3 ” ($C222_1$)	44	29
BaMnO_3	“ BaNiO_3 ” ($P6_3/mmc$)	“ KNiCl_3 ” ($P6_3cm$)	“ KNiCl_3 ” ($P6_3cm$)	115	1
LaMnO_3	rhom perov ($R - 3c$)	ortho perov ($Pnma$)	ortho perov ($Pnma$)	70	11
YMnO_3	“ LuMnO_3 ” ($P6_3cm$) \rightarrow “ Be_3N_2 ” ($P6_3/mmc$)	“ LuMnO_3 ” ($P6_3cm$)	“ LuMnO_3 ” ($P6_3cm$)	313	–
HoMnO_3	“ LuMnO_3 ” ($P6_3cm$) \rightarrow “ Be_3N_2 ” ($P6_3/mmc$)	“ LuMnO_3 ” ($P6_3cm$)	“ LuMnO_3 ” ($P6_3cm$)	364	–
LuMnO_3	“ LuMnO_3 ” ($P6_3cm$)	“ LuMnO_3 ” ($P6_3cm$)	“ LuMnO_3 ” ($P6_3cm$)	483	–
YFeO_3	ortho perov ($Pnma$)	ortho perov ($Pnma$)	ortho perov ($Pnma$)	322	–
HoFeO_3	ortho perov ($Pnma$)	ortho perov ($Pnma$)	“ LuMnO_3 ” ($P6_3cm$)	364	–
LuFeO_3	ortho perov ($Pnma$)	ortho perov ($Pnma$)	“ LuMnO_3 ” ($P6_3cm$)	493	–
LaNiO_3	rhom perov ($R\bar{3}c$)	rhom perov ($R\bar{3}c$)	rhom perov ($R\bar{3}c$)	30	–

commonly complicated by several factors: the lack of appropriate experimental data, the choice of Hubbard U in DFT+ U calculations, and the choice of crystal structure to employ in the simulation for cases where 0-K ground-state structure differs from the finite-temperature-stabilized structure observed in experiment. In the following section, we first separately address each of these factors and then present the results of the comparison.

(a) *Experimental data.* While a variety of experimental studies on examining metal oxide reduction have been conducted for solar-thermochemical applications [10–12,58–68], most of the available data focuses on hydrogen production cycles, reporting H_2 (or CO) yield and O_2 release rather than the thermodynamic quantities computed in DFT screenings [7,8,22,25,69,70]. We address this issue by selecting a number of ABO_3 compounds for synthesis and characterization. We perform thermogravimetric measurements on these compounds as a function of temperature and derive the standard state enthalpy and entropy of reduction, while also extracting structural information via *in situ* x-ray measurements. The list of compounds and crystal structures is given in Table I, and further details on the experimental measurements, techniques, and results can be found in Refs. [46,71,72].

(b) *DFT crystal structure.* In our analysis, we compare the effects of utilizing different choices of crystal structure on the DFT computed oxygen-vacancy formation energy. To do so, we compute the oxygen-vacancy formation energy utilizing four different structures (also referred to in Table I) for each of the ABO_3 compositions selected for experimental investigation:

- (1) the undistorted cubic perovskite structure in the $Pm - 3m$ space group (labelled CUB PEROV),
- (2) the lowest energy (or ground-state) structure on the OQMD at that composition (labelled DFT GS),
- (3) the crystal structure observed during experimental measurements of oxygen loss (labelled EXP),
- (4) a “dynamically stable distortion” (labelled DSD).

The reason for the introduction of the DSD structure is to address the issues arising when the EXP structure is dynamically unstable at 0 K (which will be detailed in the next paragraphs). In cases where the EXP structure is dynamically stable at 0 K, the DSD and EXP structures coincide and the results for the calculation of the EXP structure are used directly. In the cases where the EXP structure is instead dynamically unstable, a suitable alternative structure is required for the calculations. Accordingly, we identify a dynamically stable structure amongst the phases present in the OQMD at that composition with the same oxygen framework as the respective experimentally observed structure. The DSD structure is lower in energy than the EXP structure and often corresponds to the ground-state structure on the OQMD. The dynamical (in)stability of all structures is determined by performing phonon calculations as detailed in the Methods section.

In order to distinguish the effects of differences in the crystal structure from the consequences of dynamic instability, we separate the contributions to the oxygen-vacancy formation energy into two terms:

$$\Delta E_{vf} = \Delta E_{vf,UN} + \Delta E_{vf,R}. \quad (3)$$

The first term indicates the effect of removing an O atom while keeping everything else in the structure fixed, and the second term indicates the effect of letting the atoms in the structure relax once the O vacancy is introduced.

More specifically, the first term, which we call the unrelaxed contribution (UN), quantifies the DFT energy difference between a relaxed (with a relaxation of atomic positions and cell vectors performed while maintaining the symmetry of the initial structure) bulk metal oxide structure and that same structure containing the vacancy without any change in cell volume and shape or coordinates of the remaining atoms:

$$\Delta E_{vf,UN} = E_{UN}(ABO_{3-\delta}) + E_O - E_R(ABO_3). \quad (4)$$

The second term, which we refer to as a relaxation contribution (R), corresponds to the energetic change of the vacancy-containing structure when allowing for relaxation of the cell and ionic positions:

$$\Delta E_{vf,R} = E_R(ABO_{3-\delta}) - E_{UN}(ABO_{3-\delta}). \quad (5)$$

Shown in Fig. 1 are these two contributions to the oxygen-vacancy formation energy and their correlations to the structural choices in the calculations (with U values set, for convenience, to those in the OQMD). In particular, we compare the results of calculating ΔE_{vf} utilizing a cubic perovskite structure, and utilizing the DSD structure. We do so to investigate the accuracy of calculating ΔE_{vf} utilizing a cubic perovskite structure even for compounds for which such structure is not the lowest energy perovskite distortion, which, as mentioned in the introduction, is a strategy previously adopted in the literature.

We start by examining the relaxation contribution [Fig. 1(b)], as we have found this term to be significantly affected by the consequences of dynamic instability. Dynamically unstable phases do not sit in an energetic minimum, but rather at a symmetry-dictated local maximum or saddle point. When a vacancy is introduced, the symmetry of the cell is lowered and the atomic displacements which occur to accommodate the defect can change the entire structure (even far away from the defect) into a more distorted lower energy state. Hence, the energetic difference between the bulk and the defective cell is smaller than if the bulk cell had been dynamically stable. In other words, the initial bulk state being higher in energy can be seen as artificially lowering the defect formation energy. This being an effect of symmetry and atomic displacements, it arises when the defective cell is allowed to relax. Shown in Fig. 1(b) is a comparison of the relaxation contribution to the oxygen-vacancy formation energy computed for the dynamically stable distortions (y axis) and for the dynamically unstable cubic perovskite artistotypes (x axis). For all DSDs, relaxation results in an energy decrease of about 1 eV/O. In contrast, the effect for cubic perovskite structures can be of several eV/O. The effect increases with the degree of dynamic instability of the cubic perovskite structure, here defined as the energetic difference between the energy of the dynamically unstable cubic perovskite phase and the lowest energy dynamically stable perovskite distortion. Furthermore, the magnitude of the energetic decrease upon relaxation of the defect-containing structure increases not only with the degree of instability, but also with the number of atoms that move during relaxation: the larger the vacancy-containing cell, the

larger the energetic gain upon relaxation of the defective structure, and therefore the larger the lowering of ΔE_{vf} . This supercell size dependence present in dynamically unstable compounds can be understood by considering that the introduction of a vacancy results in a distortion of the entire cell, not merely locally around the vacancy. Therefore the more atoms are present in the cell, the more atoms distort upon introducing the vacancy and letting the structure relax, and the more the energy of the vacancy containing cell decreases compared to an undistorted structure with the same number of atoms. This then means that the relaxation energy $\Delta E_{vf,R}$ per O vacancy increases with the size of the vacancy containing cell. Note that this effect occurs even if constraints on the cell volume and shape are applied upon relaxation. This means that an additional and nontrivial issue involved in the use of dynamically unstable structures for defect calculations is the lack of convergence of the defect formation energy with respect to cell size, as shown in Fig. S8.

We now examine the “unrelaxed contribution,” $\Delta E_{vf,UN}$, which encapsulates effects apart from dynamic instability on ΔE_{vf} . In Fig. 1(a), we compare the $\Delta E_{vf,UN}$ between the DSD structures and cubic perovskite structures. The orthorhombic and rhombohedral perovskites have very small deviations in $\Delta E_{vf,UN}$ between the DSD and cubic perovskite. This is an indication that, in the cases where we observe a large difference in ΔE_{vf} between calculations that use a dynamically unstable cubic perovskite structure and calculations that use a dynamically stable perovskite distortion, such a difference is likely attributable to the dynamic instability of the cubic perovskite phase. For the cases where the DSD structure is a nonperovskite rather than perovskite, we observe a more significant difference in $\Delta E_{vf,UN}$ between DSD and CUBIC PEROV. The largest difference observed is for BaMnO₃ where the oxygen octahedra in the DSD structure are face-sharing, rather than corner-sharing like in perovskites. The discrepancy is also present, in smaller scale, in SrMnO₃ for which the DSD structure contains both corner- and face-sharing octahedra. These structural differences are accompanied by differences in the DFT band gap (E_g), which (from OQMD) is $E_g = 0$ for both BaMnO₃ and SrMnO₃ in the cubic perovskite phase, but nonzero in both cases for both the DSD and EXP structure, with values of 1.2 eV for “CsCuBr₃”-type SrMnO₃ and 1.1 eV for “BaMnO₃”-type SrMnO₃, and 1.9 eV for both “BaNiO₃”-type and “KNiCl₃”-type BaMnO₃. YMnO₃, HoMnO₃, and LuMnO₃, for which the difference between the unrelaxed ΔE_{vf}^{DSD} and $\Delta E_{vf}^{CUB PEROV}$ is much less pronounced, present a nonperovskite DSD structure in which the Mn cations are surrounded by polyhedra with five oxygen atoms as vertices, connected in a corner-sharing fashion, and have the same OQMD band gap in both the DSD and the cubic perovskite phase.

We also compare the relaxed and unrelaxed contributions of the DSD and EXP structures and show that the DSD surrogate structures can capture the energetics of O vacancy formation of the EXP structures without suffering from the issues of dynamic instability. In Fig. S9, we plot $\Delta E_{vf,UN}$ and $\Delta E_{vf,R}$ comparing DSD and EXP structures. In all cases, the difference in the $\Delta E_{vf,UN}$ is negligible, indicating that the DSD structures achieve the goal of capturing the ΔE_{vf} of the EXP structures when relaxation effects are not considered.

TABLE II. List of cations and “best-fit” U values determined by comparing the DFT computed oxygen-vacancy formation energy and the experimentally measured enthalpy of reduction. The U values employed in the OQMD framework are also listed for reference

Cation	Co ³⁺	Ni ³⁺	Mn ⁴⁺	Fe ³⁺	Mn ³⁺
“Best-fit” U (eV)	3	1	2	4	3
OQMD U (eV)	3.3	6.4	3.8	4	3.8

As for the relaxation component, a small difference is visible for compounds for which the EXP structure is dynamically unstable. The difference $\Delta E_{v_f,R}$ being more contained for EXP structures than for cubic perovskites can be traced back to the degree of dynamic instability being much smaller, and therefore leading to less evident lowering of ΔE_{v_f} . While on a practical level a small degree of dynamic instability does not excessively appear to impact accuracy, the previous observations about the origin of atomic relaxations away from the vacancy and the lack of convergence with cell size still caution against the use of dynamically unstable structures.

(c) *Hubbard U parameter.* Since the selected ABO_3 compounds all contain $3d$ transition metal atoms, we can assess the influence of the choice of Hubbard U parameter on the oxygen-vacancy formation energy, and identify the “best-fit” value (Table II) by comparing with experiment. In general, with the exception of Fe³⁺ which shows a very weak dependence on the U parameter, a clear negative linear trend between U and ΔE_{v_f} is visible for all compounds in Fig. 2. Furthermore, compounds containing the same element in the same oxidation state show a similar rate of decrease of ΔE_{v_f} with U and the same “best-fit” value of U . Shown in Fig. 2 are also the best-fit U values determined by comparison with experimental data (represented with horizontal banners of thickness corresponding to the value ranges given by the error bars), and the values employed in the OQMD (marked with vertical lines). While the two are in general agreement for Co³⁺, Mn³⁺, and Fe³⁺, in the case of Mn⁴⁺ and, even more visibly, Ni³⁺, OQMD U values appear to lead to a significant underestimation of the vacancy formation energy. In other words, the “best-fit” U values are in multiple cases smaller than the U values employed in the OQMD. Given the limited extent of the data set and the influence of other variables (such as the correction of the oxygen DFT reference energy) on the oxygen-vacancy formation energy, we consider this evidence to provide helpful insight to apply to our high-throughput results, but not yet sufficient to be interpreted as conclusive evidence of the optimal U values to apply to ΔE_{v_f} calculations of perovskite oxides across the board. Therefore, we conduct the high-throughput study detailed in the next section utilizing OQMD U values (changing such values would involve very substantial changes to the database), but, in recognition of the indication of the underestimation that such U values induce in the vacancy formation energy, we favor compounds with ΔE_{v_f} in the lower part of the window of interest for STCH.

(d) *Comparison between DFT and experiment.* Leveraging the insights gained in the above discussion, in Fig. 3, we test the accuracy of DFT calculations of oxygen-vacancy

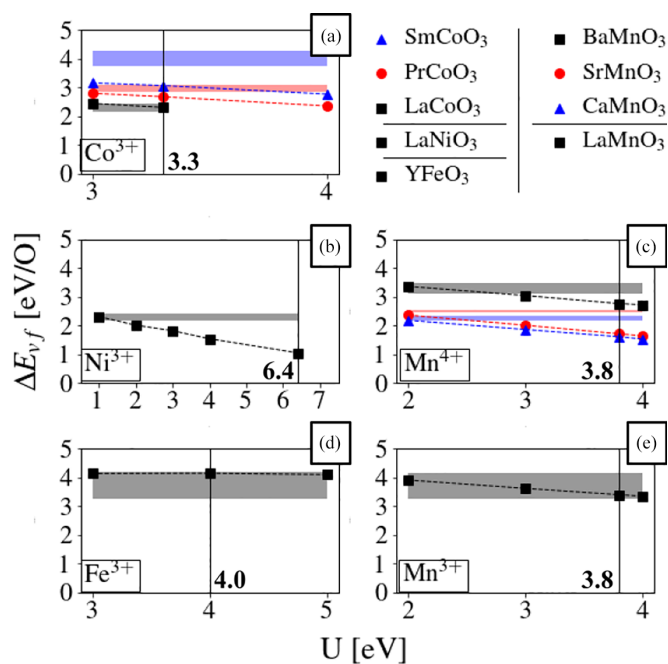


FIG. 2. Variation of the computed oxygen-vacancy formation energy with the U parameter for the ABO_3 compounds investigated for experimental comparison, for (a) $\text{LnCo}^{3+}\text{O}_3$ compounds, (b) $\text{LaNi}^{3+}\text{O}_3$, (c) $\text{AMn}^{4+}\text{O}_3$ compounds, (d) $\text{YFe}^{3+}\text{O}_3$, and (e) $\text{LaMn}^{3+}\text{O}_3$. Vertical lines indicate the value employed in the OQMD framework and horizontal banners represent experimental data, the thickness indicating the value ranges given by the error bars. DFT values are computed using the DSD structure with vacancy-containing cells of 79 atoms (119 for BaMnO_3).

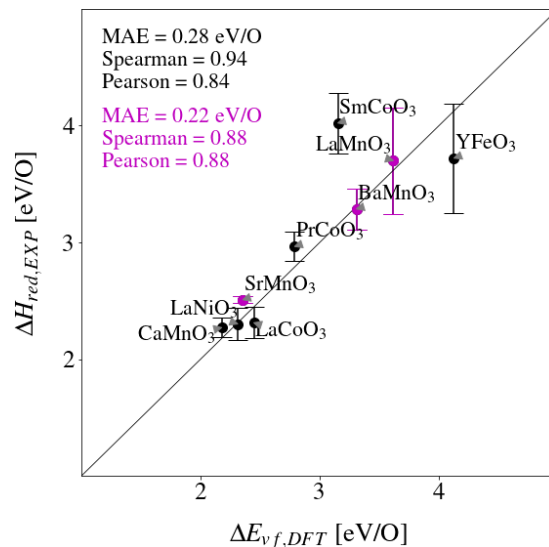


FIG. 3. Comparison of the experimental and DFT values of the oxygen-vacancy formation energy derived with best-fit U values shown in Table II. In black compounds simulated with the same structure as the experimentally measured one, in magenta compounds simulated using a dynamically stable distortion (DSD) maintaining the same type of O environment surrounding the redox-active cation as the experimentally stable structure. Vacancy-containing cell sizes are of 79 atoms (119 for BaMnO_3)

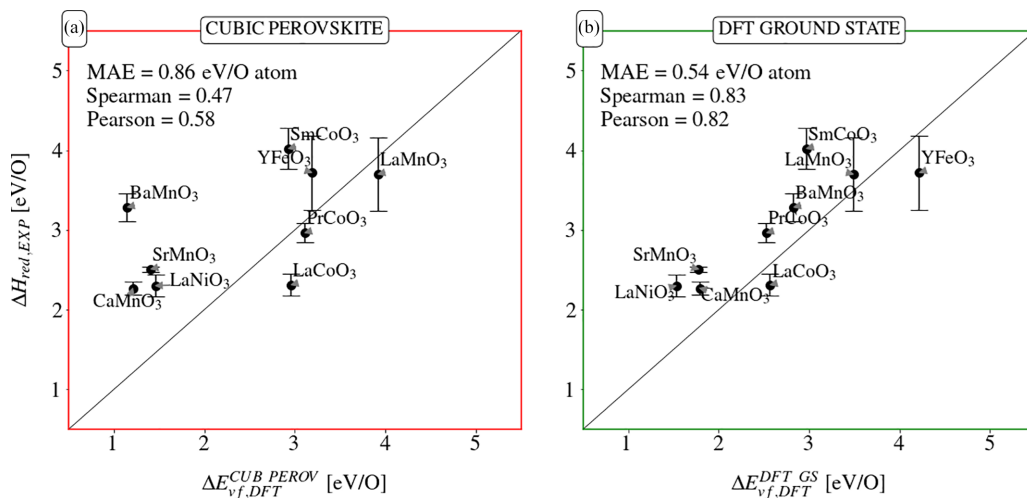


FIG. 4. Comparison experimentally derived standard enthalpies of reduction and DFT computed of the oxygen-vacancy formation energies, derived using (a) the cubic perovskite and (b) the DFT ground-state structure, both with OQMD settings, highlighting the significantly higher agreement achieved with the latter approach. U values are those implemented in the OQMD, and vacancy-containing cells are of nine atoms for cubic structures, and 19 (29 for BaMnO₃) for ground-state structures.

formation energy performed using the DSD structure and the “best-fit” U (Table II) by comparing them with the available experimentally derived enthalpies of reduction. DFT+ U calculations exhibit an accuracy comparable to experimental uncertainty and also capture the relative magnitude of the oxygen-vacancy formation energy across materials, a crucial point in material prediction. In Figs. S10 and S11, we preform the same comparison as Fig. 3 utilizing, respectively, the same Hubbard U values as the ones utilized in the OQMD, and a constant Hubbard U value of 4 eV for all compounds. In both cases, Pearson and Spearman correlation coefficients remain greater than, respectively, 0.8 and 0.9, confirming the predictive ability of the DFT ΔE_{vf} calculations in differentiating and ranking reduction enthalpies across compounds, albeit with an expected increase in the mean absolute error by approximately 0.3 eV/O.

For practical reasons such as computational expense, we used different settings for e.g. U and supercell size in our high-throughput survey (see Sec. III B) than the ones in the low-throughput study in the previous sections. These “high-throughput settings” are as follows: (i) U values from OQMD rather than “best-fit” values from previous section; (ii) lowest-energy structures at each composition, which we have argued are likely to coincide with DSD structure (this choice is further discussed in the next section); and (iii) and vacancy-containing supercells of smaller sizes than the ones used in low throughput. In order to validate the predictive power not only of the computational approach but of its high-throughput implementation as well, we separately test the agreement of the calculations performed with high-throughput settings with experiment. The relevant comparison is shown in Fig. 4, where results are contrasted between the choice of a cubic perovskite structure employed by Emery *et al.* [8] (a) and the currently proposed one of the ground-state structure (b). The underestimation of ΔE_{vf} due to dynamic instability is less dramatic when utilizing the very small nine-atom vacancy-containing cubic cell employed by Emery *et al.* [8] as compared to what is seen in Fig. 1 where 79-atom cells

were used. However, the effect is nevertheless still present, as can also be inferred from the trends in Figs. 5 and 7 presented further below. The agreement with experimental data is considerably improved when using the ground-state structure, as can be seen by a decrease in average difference between DFT computations and experimental data, despite the error not being systematically lower for every single compound. The use of the ground-state structure results in an even more significant increase in the Pearson and Spearman correlation (measuring respectively linear and monotonic character) of

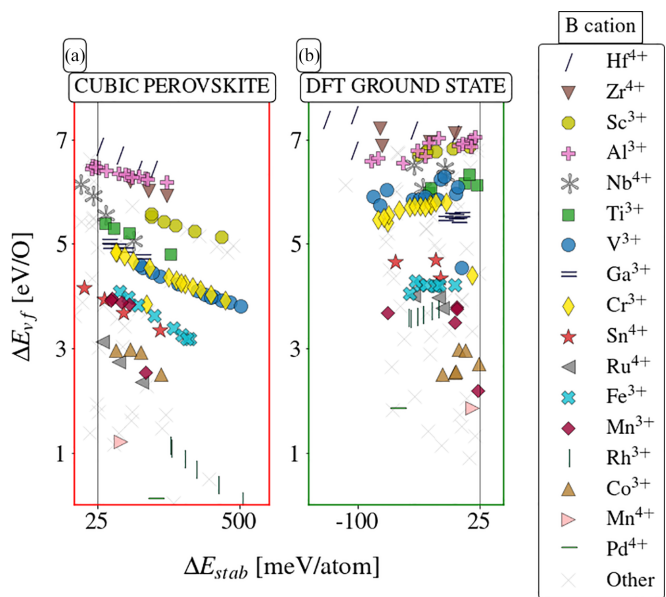


FIG. 5. Oxygen-vacancy formation energy derived using (a) the cubic perovskite structure and (b) the ground-state perovskite structure in the DFT simulations, displayed as a function of stability of the relevant structure. The left hand side clearly highlights a sharp decrease in ΔE_{vf} with increasing dynamic instability of the cubic phase. Different markers indicate different B-site cations.

the data, indicating that the high-throughput computational settings likely provide a fundamentally appropriate description of the vacancy formation energy, even though smaller nuances (such as a nonoptimal U value) still lead to an underestimation for some compounds. In addition to the calculations presented in this work, we have also examined the impact of utilizing the PBE-sol and SCAN functionals when computing the oxygen-vacancy formation energy, again for a range of Hubbard U values. These calculations were considered to be beyond the scope of the current work and are presented in a separate paper [73].

As evident from Table 1, in addition to the nine compounds illustrated in Figs. 4 and 3, thermogravimetric measurements were also performed on two orthorhombic perovskite Fe-containing compounds (LuFeO₃ and HoFeO₃) and three Mn-containing hexagonal compounds (LuMnO₃, HoMnO₃, and YMnO₃) [46]. The two ferrite compounds failed to display any significant oxygen loss upon heating; our computations agreed with this only when using the DSD structure and not the cubic (dynamically unstable) structure. As for HoMnO₃ and YMnO₃, the evidence of a phase transformation from a LuMnO₃-type structure (with $P6_3cm$ space group) to a Be₃N₂-type structure (with space group $P6_3/mmc$) was observed at higher temperatures, along with a sharp jump in the measured enthalpy (from 1.5 to 3 eV/O) and entropy (from 70 to 170 J/mol O/K) of reduction [72]. The mechanism behind the jump in the thermodynamic quantities remains ambiguous. Results from DFT stability calculations show the LuMnO₃-type structure phase to be lower in energy for all three Mn-containing hexagonal compounds, and the calculations of oxygen-vacancy formation energy performed with DSD structures (LuMnO₃-type) are in the range 3–3.5 eV/O for the three compounds.

The experimental methodology for determining the thermodynamics of oxygen-vacancy formation yields the enthalpy as a function of nonstoichiometry [49–52,74]. For the purposes of comparison to the computed results, the experimental value is defined as the average enthalpy over the range from 0 to the δ_C , the nonstoichiometry implied by the removal of one oxygen from the supercell, assuming linearity extends to δ_C . We have compared this approach with different strategies for ensuring comparison between the same physical property, such as extrapolation of the experimental value to $\delta \rightarrow 0$. Because the dependence of the experimental enthalpy on δ is relatively weak for most compounds studied here [46], the general aforementioned conclusions about the structure choice in computation and DFT prediction power remain consistent.

Overall, the evidence indicates that both the low-throughput and high-throughput approaches outlined in this work reliably predict materials reduction enthalpies accurately enough to differentiate promising candidates for STCH applications and guide experimental investigation.

B. High-throughput DFT survey of ABO₃ oxides for thermochemical water-splitting applications

After validating the efficacy of our computational approach in predicting enthalpies of reduction, we now apply it to the search for new materials for solar thermochemical (STCH) ap-

plications. This section is presented as follows: first, we detail the screening criteria for promising STCH candidates; next, we list the most promising candidates and offer larger scale evidence of the issues related to dynamic instability discussed in the previous section; and then finally, we highlight trends in ΔE_{vf} with respect to B-site cation and structural distortion.

(a) *Screening methodology.* We start with DFT data from the previous study by Emery *et al* [8], which contains stabilities of all possible ABO₃ cubic perovskites and most physically plausible distortions, as well as ΔE_{vf} calculations of the cubic perovskites. However, we extend their survey to include many additional competing nonperovskite ABO₃ structures, and, most importantly, revise the computation of the oxygen-vacancy formation energy by utilizing the ground-state structure in place of the cubic perovskite structure. To identify new promising STCH candidates we first screen for thermodynamic stability by selecting the lowest energy structure of compounds with at least one structure lying within 25 meV/atom of the convex hull. We then apply a second filter based on ΔE_{vf} values. Operation temperatures as well as the materials entropy of reduction influence the values of reduction enthalpy for which the both steps in a STCH cycle are thermodynamically favorable. Considering typical operating conditions, and keeping into account the evidence for an underestimation of the experimental ΔH_{red} in some computations of ΔE_{vf} mentioned in the previous section, we consider a ΔE_{vf} window between 2 and 5 eV/O, recognizing that even within this range, materials with $\Delta E_{vf} \geq 4$ eV/O may not undergo detectable reduction unless the entropy is extremely high (as is the case for ceria). Out of the materials in this window, we further highlight the ones containing elements lacking toxicity, radioactivity, volatility and prohibitive cost, and with ΔE_{vf} in the lower end of the window so as to allow for lower temperature of reduction.

As for the structures included in the study, the main focus remains, for the reasons outlined in the introduction, on perovskite oxides. For all compositions having a structure within 25 meV/atom from the convex hull in one of the perovskite distortions, we also computed the three other most common prototypes from the ICSD for ABO₃ compounds (see Fig. S6), and then selected the lowest energy 0-K structure considering all available phases on the OQMD at each composition. Since the Emery study [8], the OQMD has more than doubled in size to over 1 million calculations today [75,76]. This significant expansion of the database not only increases the reliability of any stability result by introducing other competing phases, but also resulted in the identification of several new stable ABO₃ metal oxide structures which are also included in the present study.

In total, we screen ~2200 compositions and ~19400 structures, selecting stable ABO₃ metal oxides and computing ΔE_{vf} of ~400 compounds. Of these, ~150 have a perovskite structure as their lowest-energy structure. From the ~400 stable compounds, we select the ~180 compounds in the 2-5eV STCH window, providing a complete list of them in Table S1.

(b) *New STCH candidates.* In Figs. 5 and 6, we show that using the ground-state perovskite structure as opposed to the cubic perovskite structure significantly changes the ΔE_{vf} results. Figure 5 highlights how the underestimation in ΔE_{vf} increases with the size of the instability of the cubic

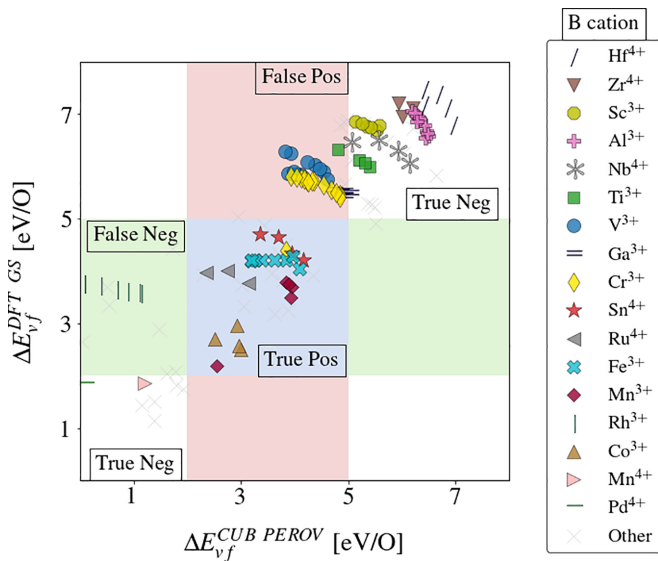


FIG. 6. Comparison of oxygen-vacancy formation energy calculated using the DFT ground-state perovskite structure on the OQMD and the cubic perovskite structure. Areas in red indicate false positives (compounds which are in the window of interest for STCH when using the cubic perovskite structure but not the ground-state structure), in green false negative (the opposite of the previous instance), and in blue true positives (compounds that would be deemed promising in both cases). Different markers indicate different B -site cations. Larger deviations from the diagonal largely correspond to compounds with a higher degree of dynamic instability of the cubic phase, as further highlighted in Fig. 5.

structure, as can be seen in the evidently descending trends in $\Delta E_{vf}^{CUB PEROV}$ with increasing ΔE_{stab} . Although ΔE_{stab} quantifies thermodynamic stability, in this case it serves as a quantification of dynamic (in)stability as well since it reports the energetic difference between the cubic phase and the phase on the convex hull, which in the majority of the cases is a distorted orthorhombic perovskite. Figure 6 demonstrates that using the ground-state structure as opposed to the cubic perovskite structure results in new promising candidates for water-splitting otherwise left out (“False Negatives”) and excludes candidates erroneously determined to be promising (“False Positives”). To be clear, “False Negatives” and “False Positives” are defined under the assumption that utilizing the ground-state structure provides a more appropriate description of the vacancy formation energy than utilizing the dynamically unstable cubic perovskite structure, as discussed in Sec. III A. Figures S13 and S14, see Ref. [42], display the same results, extended by including all nonperovskite structures present in the study as well, and highlight the same conclusions. A complete list of all stable compounds with ΔE_{stab} in the 2–5eV/O window is available in Table S1.

(c) *Trends with B-site cations.* In both Figs. 5 and 6, we highlight the influence of cation identity on oxygen-vacancy formation energy. In agreement with the previous observations by Wexler *et al.* [9] and Curnan *et al.* [28] on perovskites with $3d$ transition metal cations on the B site, we find that the B cation plays a primary role in determining ΔE_{vf} . We also find that, in the vast majority of cases, the B cation is the one

on which the majority of the charge localizes upon vacancy formation, as determined by the Bader charge analysis (see Fig. S12 and discussion in the next paragraph). Furthermore, we observe the strong correlation between cation identity and ΔE_{stab} to persist when reproducing Figs. 5 and 6 including all nonperovskite structures and highlighting the identity of the cation on which the majority of the charge localizes (which we refer to as reducing cation, see Figs. S13 and S14). This correlation can be connected to the energetic cost associated with the reduction of the cation: cations which are harder to reduce, such as Sc^{3+} lead to larger ΔE_{stab} and vice versa for easier-to-reduce cations such as Mn^{4+} . The relative trends in this energetic cost can be inferred from experimental data, for example, by looking at commonly reported oxidation states [26,27] (less common oxidation states reducing to more common ones implying a greater ease of reduction and vice versa), or at experimental measurements of reduction potentials [77]. Wexler *et al.* [9] recently introduced a quantification of the energy of reduction for each cation (and oxidation state) incorporating crystal field effects by leveraging differences in formation energies between structures containing the cation of interest in the initial and reduced oxidation state.

The charge localization on A - and B -site cations (Δq) upon oxygen-vacancy formation in perovskites is illustrated in Fig. S12. In the majority of the cases, rare-earth and alkaline earth metals are on the A site, both groups having significantly larger reduction energies than the transition metals, which largely occupy the B sites. Unsurprisingly, in the vast majority of cases most of the charge localizes on the B site cations upon oxygen-vacancy formation (i.e., we identify the B site cation as the reducing cation). In cases where a cation which is easier to reduce, such as Bi^{3+} , occupies the A site, a significant lowering of ΔE_{vf} compared to other compounds with the same B site cation can be observed, accompanied by a larger charge localization on the A site cation. In such cases (e.g., $BiVO_3$, $BiCrO_3$, $BiMnO_3$, and $TeFeO_3$) evidence for reduction on both sites can be observed, with $BiVO_3$ going as far as having most charge localizing on the A site cation. A suggestion of reduction of both A and B cations with Bi^{3+} on the A site was also put forth by Wexler *et al.* [9] and can represent a desirable property as it would lead to an increase in the entropy change involved in the reduction reaction, and thus to a more favorable STCH cycle [7,24].

When considering ΔE_{vf} in the lower end of the STCH window, availability and lack of prohibitive cost or toxicity, Mn^{4+} , Mn^{3+} , and Co^{3+} emerge as the most promising redox-active cations for STCH applications (see Table III), although we do note that our investigations of $REMnO_3$ ($YMnO_3$, $LuMnO_3$, and $HoMnO_3$) suggest higher temperatures to be needed to reduce $LuMnO_3$ type compounds [46]. Co^{3+} and Mn^{3+} have also been highlighted as promising B site cations in perovskites in the recent work by Wexler *et al.* [9], despite differences in the specific predicted values probably due to the differences in exchange correlation functional and Hubbard U , and in the structures included in the study. While Mn^{4+} displays a rather low reduction enthalpy in perovskites, making it less attractive as the sole B -site element [71], the oxygen-vacancy formation energy can be increased by introduction of substitutional elements on the B site. We synthesized two Mn^{4+} -based mixed perovskites and, encouragingly, found

TABLE III. Promising compounds for STCH applications: composition, ground-state structure (with the same naming convention utilized in Table I), *B*-site cation, and oxygen-vacancy formation energy. Compounds that were analyzed in Sec. III A are in parenthesis, here reported to show they satisfy screening criteria.

Composition	Structure	<i>B</i> -Site Cation	ΔE_{vf} eV/O
(PrCoO ₃)	ortho perov (<i>Pnma</i>)	Co ³⁺	2.7
(LaCoO ₃)	monocl perov (<i>P2₁/c</i>)		2.7
NdCoO ₃	ortho perov (<i>Pnma</i>)		3.0
TbCoO ₃	ortho perov (<i>Pnma</i>)		3.0
(SmCoO ₃)	ortho perov (<i>Pnma</i>)		3.5
(BaMnO ₃)	“KNiCl ₃ ” (<i>P6₃cm</i>)	Mn ⁴⁺	2.8
ScMnO ₃	“LuMnO ₃ ” (<i>P6₃cm</i>)	Mn ³⁺	3.3
TmMnO ₃	“LuMnO ₃ ” (<i>P6₃cm</i>)		3.4
TbMnO ₃	“LuMnO ₃ ” (<i>P6₃cm</i>)		3.4

these to display favourable redox thermodynamics and high fuel production upon cycling [78,79]. Attractive redox values for Mn³⁺ and Mn⁴⁺ were also previously reported in the work by Vieten *et al.* analyzing several mixed perovskites [23]. Among the other common *B* cation metal oxide elements identified in the study not suffering from particular cost and toxicity concerns, V³⁺, Ti³⁺, and Cr³⁺ all appear to be too hard to reduce for STCH applications and Ni³⁺ potentially too easy. Lastly, while several Fe³⁺-containing compounds display ΔE_{vf} values in the 2–5 eV STHC window, such values all lie above 4 eV/O, and Fe³⁺, previously suggested as an attractive cation by Wexler *et al.* [9], is considered less likely to be promising candidate, as supported by the experimental observation of very limited if not entirely absent oxygen loss previously mentioned in the experimentally synthesized perovskite ferrite compounds.

(*d*) Trends with perovskite structural distortion. For the vast majority of the stable perovskites identified in this study, the ground-state structure is a distortion of lower symmetry than the perfect cubic phase. An especially convenient metric to estimate the degree of structural distortion, given its simplicity and ease of computation, is the Goldschmidt tolerance factor [80]:

$$\text{tolerance} = \frac{r_A + r_O}{\sqrt{2}(r_B + r_O)}, \quad (6)$$

In Fig. 7, we show how this metric, which is often used to predict the structure and synthesizability of a perovskite composition, can also capture two contrasting behaviours in the oxygen-vacancy formation energy of perovskites when using the ground-state versus the cubic structure. On the one hand, an inverse correlation with tolerance can be observed when utilizing ground-state structure, in agreement with observations of compressive strain increasing the oxygen-vacancy formation energy [81]. As rare-earth cations occupy the *A* site in the majority of the *ABO*₃ perovskites here analyzed, for the same *B* cation, higher values of the tolerance factor are associated with earlier rare-earth *A* cations, and lower values with later rare-earth *A* cations. The more distorted structures of perovskites that contain later rare-earth *A* cations are characterized by higher values of the vacancy formation

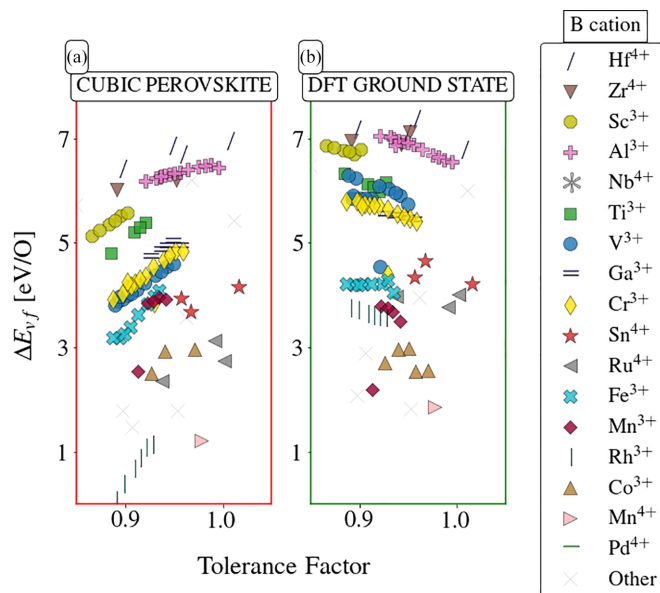


FIG. 7. Oxygen-vacancy formation energy derived using (a) the cubic structure and (b) the ground-state structure in the DFT simulations, displayed as a function of the tolerance factor computed using a bond valence method [83]. Different markers and colors symbolize different *B*-site cations and oxidation states.

energy compared to other perovskites with the same *B* cation. They are also characterized by higher values of the magnetic moment of the *B* cation, indicating a decrease in the covalent character of the *B*-O bond, a behavior similar to what observed by Varignon *et al.* [82] in Ni-based perovskites. In contrast, when the cubic structure is utilized, the observed trend is reversed, i.e., higher values of the tolerance factor are associated with higher values of the vacancy formation energy for compounds containing the same *B* cation, a behavior that can be attributed once again to its dynamic instability. The more distorted the ground-state structure, the larger the distance of the cubic structure from the energetic landscape minimum, and thus the larger the underestimation of ΔE_{vf} when using the cubic structure.

IV. CONCLUSION

In the present work, we determine an effective computational description of the enthalpy associated with oxygen release from a metal oxide, and use it to predict materials for solar thermochemical water-splitting applications in a high-throughput fashion. We first examine the impact of crystal structure and demonstrate that the employment of a dynamically unstable structure in DFT simulations leads to an artificial lowering of the oxygen-vacancy formation energy. We address cases with a dynamically unstable experimentally observed structure by identifying and employing a dynamically stable structure preserving the same oxygen framework of the original structure of interest. We then demonstrate the effectiveness of our computational approach in capturing the physical processes involved in the creation of oxygen vacancies through comparison with experimental data of reduction enthalpies for a set of *ABO*₃ compounds. Through

successful comparison with experimental results, we confirm the use of high-throughput DFT to produce sufficiently accurate quantitative predictions of ΔE_{vf} to guide experiment in the search for novel materials for STCH applications. Concentrating on perovskite oxides and including other common ABO_3 structures, we thereby conduct such high-throughput study, highlighting the substantial dependence of ΔE_{vf} on the redox-active cation, and identifying Mn^{4+} , Mn^{3+} , and Co^{3+} as the most promising ones.

ACKNOWLEDGMENTS

This work was funded by the U.S. Department of Energy under Grant No. DE-EE0008089 (DFT calculations,

Quantitative comparison with experiment, High-throughput calculations). S.G. acknowledges funding from the U.S. Department of Commerce and National Institute of Standards and Technology as part of the Center for Hierarchical Materials Design (ChiMaD) under Award No. 70NANB19H005 (OQMD calculations and high-throughput workflow). The high-throughput data was produced relying on the computing power provided by Quest high performance computing facility at Northwestern University, while the calculations used for experimental comparison were performed utilizing computational resources at the National Energy Research Scientific Computing Center (NERSC) under Contract No. DE-AC02-05CH11231, a U.S. Department of Energy Office of Science User Facility.

-
- [1] S. B. Adler, *Chem. Rev.* **104**, 4791 (2004).
- [2] J. A. Kilner and M. Burriel, *Annu. Rev. Mater. Res.* **44**, 365 (2014).
- [3] B. Bulfin, J. Vieten, C. Agrafiotis, M. Roeb, and C. Sattler, Applications and limitations of two step metal oxide thermochemical redox cycles; a review, *J. Mater. Chem. A*, **5**, 18951 (2017).
- [4] T. Nakamura, *Solar Energy* **19**, 467 (1977).
- [5] Z. Wang, R. Roberts, G. Naterer, and K. Gabriel, *Int. J. Hydrogen Energy* **37**, 16287 (2012).
- [6] W. C. Chueh, C. Falter, M. Abbott, D. Scipio, P. Furler, S. M. Haile, and A. Steinfeld, *Science* **330**, 1797 (2010).
- [7] B. Meredig and C. Wolverton, *Phys. Rev. B* **80**, 245119 (2014).
- [8] A. A. Emery, J. E. Saal, S. Kirklin, V. I. Hegde, and C. Wolverton, *Chem. Mater.* **28**, 5621 (2016).
- [9] R. B. Wexler, G. S. Gautam, E. B. Stechel, and E. A. Carter, *J. Am. Chem. Soc.* **143**, 13212 (2021).
- [10] A. H. McDaniel, E. C. Miller, D. Arifin, A. Ambrosini, E. N. Coker, R. O'Hayre, W. Chueh, and J. Tong, *Energy Environ. Sci.* **6**, 2424 (2013).
- [11] J. R. Scheffe, D. Weibel, and A. Steinfeld, *Energy Fuels* **27**, 4250 (2013).
- [12] A. McDaniel, A. Ambrosini, E. Coker, J. Miller, W. Chueh, R. O'Hayre, and J. Tong, *Energy Procedia* **49**, 2009 (2014).
- [13] C. K. Yang, Y. Yamazaki, A. Aydin, and S. M. Haile, *J. Mater. Chem. A* **2**, 13612 (2014).
- [14] J. R. Scheffe and A. Steinfeld, *Mater. Today* **17**, 341 (2014).
- [15] A. Demont, S. Abanades, and E. Beche, *J. Phys. Chem. C* **118**, 12682 (2014).
- [16] J. Breternitz and S. Schorr, *Adv. Energy Mater.* **8**, 1802366 (2018).
- [17] B. J. Kennedy and B. A. Hunter, *Phys. Rev. B* **58**, 653 (1998).
- [18] B. J. Kennedy, C. J. Howard, and B. C. Chakoumakos, *Phys. Rev. B* **59**, 4023 (1999).
- [19] B. J. Kennedy, C. J. Howard, and B. C. Chakoumakos, *Phys. Rev. B* **60**, 2972 (1999).
- [20] C. J. Howard, K. S. Knight, B. J. Kennedy, and E. H. Kisi, *J. Phys.: Condens. Matter* **12**, L677 (2000).
- [21] K. Knight, *Solid State Ionics* **74**, 109 (1994).
- [22] M. Ezbiri, M. Takacs, B. Stolz, J. Lungthok, A. Steinfeld, and R. Michalsky, *J. Mater. Chem. A* **5**, 15105 (2017).
- [23] J. Vieten, B. Bulfin, P. Huck, M. Horton, D. Guban, L. Zhu, Y. Lu, K. A. Persson, M. Roeb, and C. Sattler, *Energy Environ. Sci.* **12**, 1369 (2019).
- [24] G. Sai Gautam, E. B. Stechel, and E. A. Carter, *Chem. Mater.* **32**, 9964 (2020).
- [25] A. M. Deml, A. M. Holder, R. P. O'Hayre, C. B. Musgrave, and V. Stevanovic, *J. Phys. Chem. Lett.* **6**, 1948 (2015).
- [26] G. Bergerhoff, R. Hundt, R. Sievers, and I. D. Brown, The inorganic crystal structure data base, *J. Chem. Inf. Comp. Sci.* **23**, 66 (1983).
- [27] A. Belsky, M. Hellenbrandt, V. L. Karen, and P. Luksch, *Acta Crystallogr. Sect. B: Struct. Sci.* **58**, 364 (2002).
- [28] M. T. Curnan and J. R. Kitchin, *J. Phys. Chem. C* **118**, 28776 (2014).
- [29] S. L. Dudarev, G. A. Botton, S. Y. Savrasov, C. J. Humphreys, and A. P. Sutton, *Phys. Rev. B* **57**, 1505 (1998).
- [30] B. Himmetoglu, A. Floris, S. de Gironcoli, and M. Cococcioni, *Int. J. Quantum Chem.* **114**, 14 (2014).
- [31] F. Zhou, M. Cococcioni, C. A. Marianetti, D. Morgan, and G. Ceder, *Phys. Rev. B* **70**, 235121 (2004).
- [32] L. Wang, T. Maxisch, and G. Ceder, *Phys. Rev. B* **73**, 195107 (2006).
- [33] S. Lutfalla, V. Shapovalov, and A. T. Bell, *J. Chem. Theory Comput.* **7**, 2218 (2011).
- [34] V. L. Chevrier, S. P. Ong, R. Armiento, M. K. Y. Chan, and G. Ceder, *Phys. Rev. B* **82**, 075122 (2010).
- [35] M. Aykol and C. Wolverton, *Phys. Rev. B* **90**, 115105 (2014).
- [36] O. Y. Long, G. Sai Gautam, and E. A. Carter, *Phys. Rev. Mater.* **4**, 045401 (2020).
- [37] G. Sai Gautam and E. A. Carter, *Phys. Rev. Mater.* **2**, 095401 (2018).
- [38] G. Kresse and J. Furthmuller, *Comput. Mater. Sci.* **6**, 15 (1996).
- [39] G. Kresse and J. Furthmuller, *Phys. Rev. B* **54**, 11169 (1996).
- [40] G. Kresse and D. Joubert, *Phys. Rev. B* **59**, 1758 (1999).
- [41] J. P. Perdew, K. Burke, and M. Ernzerhof, *Phys. Rev. Lett.* **77**, 3865 (1996).
- [42] See Supplemental Material at <http://link.aps.org/supplemental/10.1103/PhysRevMaterials.7.065403> for additional information on DFT calculations and results.
- [43] J. E. Saal, S. Kirklin, M. Aykol, B. Meredig, and C. Wolverton, *JOM* **65**, 1501 (2013).

- [44] S. Kirklin, J. E. Saal, B. Meredig, A. Thompson, J. W. Doak, M. Aykol, S. Rühl, and C. Wolverton, *npj Comput. Mater.* **1**, 15010 (2015).
- [45] S. P. Ong, W. D. Richards, A. Jain, G. Hautier, M. Kocher, S. Cholia, D. Gunter, V. L. Chevrier, K. A. Persson, and G. Ceder, *Comput. Mater. Sci.* **68**, 314 (2013).
- [46] X. Qian, Nonstoichiometric perovskite oxides for solar-driven thermochemical water splitting, Ph.D. thesis, Northwestern University, 2021.
- [47] E. Mastronardo, X. Qian, J. M. Coronado, and S. M. Haile, *Journal of Energy Storage* **40**, 102793 (2021).
- [48] Y.-L. Lee, J. Kleis, J. Rossmeisl, and D. Morgan, *Phys. Rev. B* **80**, 224101 (2009).
- [49] J. Kuo, H. Anderson, and D. Sparlin, *J. Solid State Chem.* **83**, 52 (1989).
- [50] J. Nowotny and M. Rekas, *J. Am. Ceram. Soc.* **81**, 67 (1998).
- [51] J. Mizusaki, M. Yoshihiro, S. Yamauchi, and K. Fueki, *J. Solid State Chem.* **58**, 257 (1985).
- [52] J. Mizusaki, Y. Mima, S. Yamauchi, K. Fueki, and H. Tagawa, *J. Solid State Chem.* **80**, 102 (1989).
- [53] E. Bucher, W. Sitte, G. Caraman, V. Cherepanov, T. Aksenova, and M. Ananyev, *Solid State Ionics* **177**, 3109 (2006).
- [54] A. Jain, G. Hautier, S. P. Ong, C. J. Moore, C. C. Fischer, K. A. Persson, and G. Ceder, *Phys. Rev. B* **84**, 045115 (2011).
- [55] S. Grindy, B. Meredig, S. Kirklin, J. E. Saal, and C. Wolverton, *Phys. Rev. B* **87**, 075150 (2013).
- [56] V. Stevanovic, S. Lany, X. Zhang, and A. Zunger, *Phys. Rev. B* **85**, 115104 (2012).
- [57] A. Togo and I. Tanaka, *Scr. Mater.* **108**, 1 (2015).
- [58] L. Nalbandian, A. Evdou, and V. Zaspalis, *Int. J. Hydrogen Energy* **34**, 7162 (2009).
- [59] T. Kodama, Y. Nakamuro, and T. Mizuno, *J. Solar Energy Engineering, Transactions of the ASME* **128**, 3 (2006).
- [60] S. Dey, B. S. Naidu, and C. N. Rao, *Chemistry - A European Journal* **21**, 7077 (2015).
- [61] S. Dey, B. S. Naidu, A. Govindaraj, and C. N. Rao, *Phys. Chem. Chem. Phys.* **17**, 122 (2015).
- [62] D. Okeefe, C. Allen, G. Besenbruch, L. Brown, J. Norman, R. Sharp, and K. McCorkle, *Int. J. Hydrogen Energy* **7**, 381 (1982).
- [63] A. Le Gal and S. Abanades, *J. Phys. Chem. C* **116**, 13516 (2012).
- [64] A. H. Bork, M. Kubicek, M. Struzik, and J. L. Rupp, *Journal of Materials Chemistry A* **3**, 15546 (2015).
- [65] L. Wang, M. Al-Mamun, P. Liu, Y. Wang, H. G. Yang, and H. Zhao, *Chinese Journal of Catalysis* **38**, 1079 (2017).
- [66] L. Wang, M. Al-Mamun, P. Liu, Y. Wang, H. G. Yang, and H. Zhao, *J. Mater. Sci.* **53**, 6796 (2018).
- [67] F. He and F. Li, *Energy Environ. Sci.* **8**, 535 (2015).
- [68] M. Orfila, M. Linares, R. Molina, J. Á. Botas, R. Sanz, and J. Marugán, *Int. J. Hydrogen Energy* **41**, 19329 (2016).
- [69] A. M. Deml, V. Stevanovic, C. L. Muhich, C. B. Musgrave, and R. O'Hayre, *Energy Environ. Sci.* **7**, 1996 (2014).
- [70] R. Michalsky, V. Botu, C. M. Hargus, A. A. Peterson, and A. Steinfeld, *Adv. Energy Mater.* **5**, 1401082 (2015).
- [71] E. Mastronardo, X. Qian, J. M. Coronado, and S. M. Haile, *J. Mater. Chem. A* **8**, 8503 (2020).
- [72] X. Qian, S. M. Haile, T. C. Davenport, and E. Mastronardo, *J. Am. Ceram. Soc.* **105**, 4375 (2022).
- [73] J. He, B. Baldassarri, and C. Wolverton, Assessment of exchange-correlation functionals on oxygen vacancy formation energies of metal oxides (unpublished).
- [74] Y. Hao, C.-K. Yang, and S. M. Haile, *Chem. Mater.* **26**, 6073 (2014).
- [75] H.-C. Wang, S. Botti, and M. A. L. Marques, Predicting stable crystalline compounds using chemical similarity, *npj Comput. Mater.* **7** (2021).
- [76] J. Shen, S. Griesemer, A. Gopakumar, B. Baldassarri, J. E. Saal, M. Aykol, V. Hegde, and C. Wolverton, *J. Phys.: Mater.* **5**, 031001 (2022).
- [77] *CRC Handbook of Chemistry and Physics*, 87th ed. (CRC Press/Taylor and Francis Group: Boca Raton, FL, 2006).
- [78] X. Qian, J. He, E. Mastronardo, B. Baldassarri, C. Wolverton, and S. M. Haile, *Chem. Mater.* **32**, 9335 (2020).
- [79] X. Qian, J. He, E. Mastronardo, B. Baldassarri, W. Yuan, C. Wolverton, and S. M. Haile, *Matter* **4**, 688 (2021).
- [80] V. M. Goldschmidt, *Naturwissenschaften* **14**, 477 (1926).
- [81] H. A. Tahini, X. Tan, U. Schwingenschlögl, and S. C. Smith, *ACS Catal.* **6**, 5565 (2016).
- [82] J. Varignon, M. Grisolia, and J. Iniguez, *npj Quant Mater* **2**, 21 (2017).
- [83] M. W. Lufaso and P. M. Woodward, *Acta Crystallogr B Struct Sci* **57**, 725 (2001).